

Transformation from Magnetic Soliton to Skyrmion in a Monoaxial Chiral Magnet

Long Li, Dongsheng Song,* Weiwei Wang,* Fengshan Zheng, András Kovács, Mingliang Tian, Rafal E. Dunin-Borkowski, and Haifeng Du*

Topological spin textures are of great interest for both fundamental physics and applications in spintronics. The Dzyaloshinskii–Moriya interaction underpins the formation of single-twisted magnetic solitons or multi-twisted magnetic skyrmions in magnetic materials with different crystallographic symmetries. However, topological transitions between these two kinds of topological objects have not been verified experimentally. Here, the direct observation of transformations from a chiral soliton lattice (CSL) to magnetic skyrmions in a nanostripe of the monoaxial chiral magnet CrNb_3S_6 using Lorentz transmission electron microscopy is reported. In the presence of an external magnetic field, helical spin structures first transform into CSLs and then evolve into isolated elongated magnetic skyrmions. The detailed spin textures of the elongated magnetic skyrmions are resolved using off-axis electron holography and are shown to comprise two merons, which enclose their ends and have unit total topological charge. Magnetic dipolar interactions are shown to play a key role in the magnetic soliton–skyrmion transformation, which depends sensitively on nanostripe width. The findings here, which are consistent with micromagnetic simulations, enrich the family of topological magnetic states and their transitions and promise to further stimulate the exploration of their emergent electro-magnetic properties.

1. Introduction

In magnetic materials with different crystallographic symmetries, a delicate interplay between the Dzyaloshinskii–Moriya (DM) interaction^[1,2] and the Heisenberg exchange interaction can result in the formation of periodically modulated topological spin textures that are mediated by the Zeeman effect.^[3] The DM interaction, which results from broken crystal inversion symmetry,^[4,5] can be expressed in the form^[6] $H_{\text{DM}} = D_{12} \cdot (S_1 \times S_2)$, where S_1 and S_2 are neighboring atomic spins and the DM vector D_{12} is intrinsic to chiral magnetic crystals, whose symmetries dictate the vector direction. A 1D DM vector can generate magnetic solitons in chiral helimagnetic (CHM) crystals, such as CrNb_3S_6 ,^[7] MnNb_3S_6 ,^[8,9] and CrTa_3S_6 ,^[10] whereas a multi-dimensional DM vector can generate a variety of magnetic states in acentric chiral magnets, such as magnetic skyrmions,^[11,12] chiral bobsbers,^[13,14] magnetic bundles,^[15,16] and antiskyrmions.^[17]

L. Li, D. Song, W. Wang, M. Tian, H. Du
Anhui Key Laboratory of Condensed Matter Physics at Extreme Conditions
High Magnetic Field Laboratory
HFIPS
Chinese Academy of Sciences
Hefei, Anhui 230031, P. R. China
E-mail: dsong@ahu.edu.cn; wangweiwei@ahu.edu.cn; duhf@hmfl.ac.cn

L. Li, M. Tian, H. Du
Science Island Branch of Graduate School
University of Science and Technology of China
Hefei, Anhui 230026, P. R. China

D. Song, W. Wang, H. Du
Information Materials and Intelligent Sensing Laboratory of Anhui Province
Key Laboratory of Structure and Functional Regulation of Hybrid Materials of Ministry of Education
Institutes of Physical Science and Information Technology
Anhui University
Hefei, Anhui 230601, P. R. China

D. Song, F. Zheng, A. Kovács, R. E. Dunin-Borkowski
Ernst Ruska-Centre for Microscopy and Spectroscopy with Electrons and Peter Grünberg Institute
Forschungszentrum Jülich
52425 Jülich, Germany

F. Zheng
Spin-X Institute
Electron Microscopy Center
School of Physics and Optoelectronics
State Key Laboratory of Luminescent Materials and Devices
Guangdong-Hong Kong-Macao Joint Laboratory of Optoelectronic and Magnetic Functional Materials
South China University of Technology
Guangzhou 510006, P. R. China

M. Tian
School of Physics and Optoelectronics Engineering
Anhui University
Hefei, Anhui 230601, P. R. China

 The ORCID identification number(s) for the author(s) of this article can be found under <https://doi.org/10.1002/adma.202209798>.

DOI: 10.1002/adma.202209798

These topological objects exhibit rich electromagnetic properties and have been considered for future spintronic devices.^[18] Transitions between spin textures with different topological magnetic orders in chiral magnets include skyrmions and antiskyrmions,^[19–21] skyrmions and merons,^[22] skyrmions and bubbles,^[23] and antiskyrmions and bubbles,^[19,20] suggesting their applications in magnetic solid-state memory devices, in which streams of binary data bits are encoded by sequences of two different objects. However, continuous transformations are generally not favorable between topological spin textures that originate from different types of DM vectors, such as skyrmions in monoaxial chiral magnets, as a result of the constraint of crystal symmetry.

Here, we use Lorentz transmission electron microscopy (LTEM) to directly observe a topological phase transition from magnetic solitons to new types of skyrmions, which are highly elongated and have unit topological charge, in CrNb₃S₆ monoaxial crystals that have confined geometries. The elongated skyrmions can be sustained over specific ranges of external magnetic field and temperature, with topologically distorted geometrical shapes. We resolve the fine magnetic structures of the elongated skyrmions using off-axis electron holography and study the dependence of the magnetic transition on nanostructure width. We use micromagnetic simulations to show that dipolar–dipolar interactions are responsible for the stabilization of the skyrmion phase in such magnetic soliton crystals.

2. Results and Discussions

In skyrmion-hosting chiral magnets, such as FeGe,^[24] FeCoSi,^[12] MnSi,^[11] and Cu₂OSeO₃,^[25] Bloch-type skyrmions are generally formed from chiral helical textures in the presence of an external magnetic field, as shown in Figure 1. 2D skyrmion lattices are stabilized by a competition between ferromagnetic exchange and DM interactions. In comparison, in magnetic-soliton-hosting CHM crystals, such as CrNb₃S₆,^[26,27] chiral helical textures are transformed into 1D chiral soliton lattices (CSLs)^[7,28–32] along the helical axis (*z* direction) in the presence of an external magnetic field (*x* direction), as shown in Figure 1b, as a result of the monoaxial DM interaction. CSLs are separated by ferromagnetic domains and have periodicities that increase non-monotonically with applied field, exhibiting strong coupling with conduction electrons and giving rise to nontrivial magneto-transport properties.^[30,33–42] The magnetic skyrmion states most commonly exist in cubic crystals with magnetic isotropy, while the magnetic soliton states are formed in hexagonal crystals with uniaxial magnetic anisotropy. Transformations from 1D solitons to 2D skyrmions are therefore typically restricted by the intrinsic crystal structure and the resulting different types of DM vectors. However, this behavior is observed in systems that have infinite size. In contrast, in a sample that has a fixed geometry, boundary conditions may result in confinement effects on topological spin textures and in the formation of twisted magnetic structures, such as magnetic skyrmions with elliptically distorted shapes in nanostripes.^[43] Similar considerations are anticipated for transformations between magnetic solitons and skyrmions, as shown in Figure 1b,c.

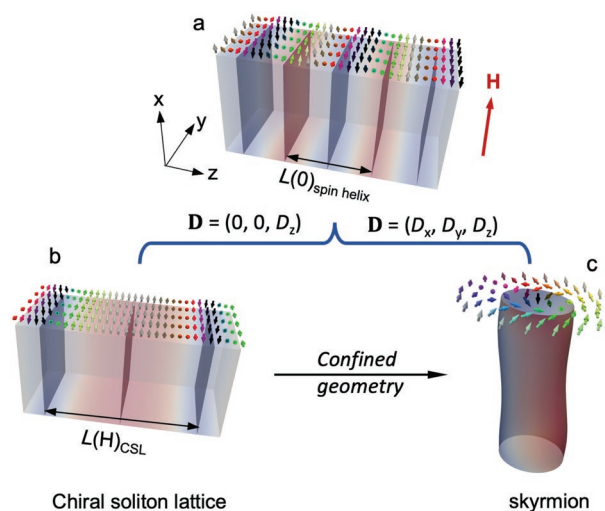


Figure 1. Schematic diagram of transformations between different spin textures. a) Representative spin texture of a chiral helical stripe in a ground state at $H = 0$ mT. The period of the spin helix stripe is $L(0)$. b) Chiral soliton lattice (CSL) stabilized by a monoaxial DM vector in an external field H along the x -direction. The period of the CSL is $L(H)$ and the helical axis is along z direction. c) Formation of a magnetic skyrmion with multidimensional DM vectors in an external field. The skyrmion has unit topological charge. The CSL is anticipated to transform into skyrmion in a geometrically confined system.

In order to systematically investigate the CSL to skyrmion transformation in a confined geometry experimentally, we studied the archetypal magnetic soliton crystal CrNb₃S₆. A CrNb₃S₆ nanostripe was fabricated using focused Ga ion beam milling by the traditional lift-out technique, as described in the Experimental Section. The helical axis was oriented along the long side of the nanostripe to ensure a vertical arrangement of CSLs. Figure 2a shows a defocused LTEM image of a CrNb₃S₆ nanostripe that has a width of $\approx 1 \mu\text{m}$ and a thickness of ≈ 150 nm. The image shows magnetic contrast with a periodicity of ≈ 48 nm in zero magnetic field ($H = 0$) at a temperature of $T = 95$ K, corresponding to a CHM phase, in agreement with previous results.^[7,30,44,45] When the external magnetic field is perpendicular to the helical axis (in the out-of-plane direction), the incommensurate CHM phase transforms into the CSL phase at $H = 176$ mT, as shown in Figure 2b. The number of helical stripes decreases and the spacing of neighboring stripes increases, corresponding to the formation of a CSL with a larger periodicity, while some of the solitons break away from the two edges. As the magnetic field is increased to 198 mT, the periodicity of the CSL becomes much greater. Most of the solitons have now escaped from the two edges and disconnected solitons have formed, as shown in Figure 2c. The lengths of the disconnected solitons in the vertical direction range from tens to hundreds of nm. On increasing the magnetic field further, the disconnected solitons decrease in size, becoming smaller than 50 nm at $H = 211$ mT, as shown in Figure 2d. When the external magnetic field reaches $H = 225$ mT, all of the disconnected solitons have disappeared and the nanostripe is saturated ferromagnetically.

Off-axis electron holography was used to resolve the magnetic structures of the disconnected solitons with high spatial resolution and high magnetic sensitivity.^[46] The details of the

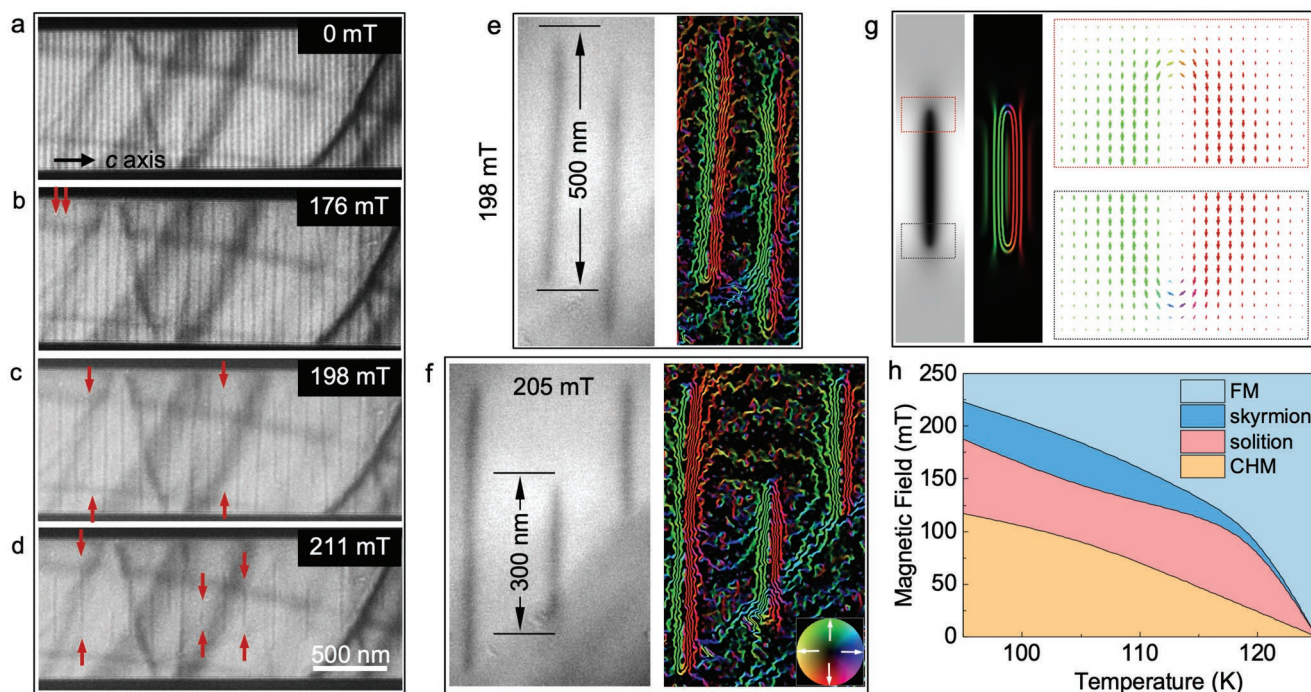


Figure 2. Experimental observations of the transformation from a magnetic soliton lattice to a magnetic skyrmion in a CrNb_3S_6 nanostructure. a) Representative helical stripes in a nanostructure in zero magnetic field. The magnetic contrast is sinusoidal and has a period of ≈ 48 nm. The width of the nanostructure is ≈ 1 μm . The crystallographic c axis is marked by a black arrow in the horizontal direction. b–d) Magnetic-field-dependent evolution of magnetic spin texture from helical stripes to CSLs and elongated skyrmions with increasing magnetic field applied in the out-of-plane direction. Some of the disconnected solitons are indicated by the red arrows to guide the eye. The left panels in (e) and (f) show experimental magnetic phase shift images of elongated skyrmions recorded using off-axis electron holography. Their lengths are marked by black arrows. The right panels show corresponding magnetic induction maps with contour spacings of $2\pi/100 = 0.0628$ rad. g) Simulated magnetic phase shift image and corresponding magnetic induction map based on the spin texture of an elongated skyrmion from micromagnetic simulations shown in Figure 3a. The red dotted boxes show magnetic vectors at the upper and lower ends of the elongated skyrmion. h) Magnetic phase diagram plotted as a function of magnetic field and temperature. The Curie temperature of CrNb_3S_6 is estimated to be ≈ 125 K.

measurements can be found in the Experimental Section. Representative magnetic phase images recorded at 95 K are shown in the left panels of Figure 2e,f for applied magnetic fields of 198 and 205 mT, respectively. The disconnected solitons exhibit flux-closed magnetic structures, with continuous transitions in magnetic induction at their upper and lower edges. Around the disconnected solitons, the lack of magnetic phase contours is consistent with a ferromagnetic state with out-of-plane magnetization. Each disconnected soliton can be regarded as an elongated skyrmion, whose ends are enclosed by two merons, with unit total topological charge. It should be noted that the sizes of the elongated skyrmions can be varied by using the external magnetic field, in contrast to Bloch-type skyrmions^[3] with an intrinsic size. In order to confirm the interpretation of the observed magnetic structures, magnetic phase images were simulated based on the micromagnetic simulations shown later in Figure 4a. The simulations shown in Figure 2g reproduce the experimental results shown in Figure 2e,f closely.

A phase diagram showing the temperature and magnetic field dependence of the magnetic transition in the nanostructure is shown in Figure 2h. The value of T_C for the CrNb_3S_6 nanostructure is estimated to be ≈ 125 K from the phase diagram, which is comparable to that of the bulk magnet.^[27] As the magnetic field is increased, the CHM phase transforms into a CSL. Before transforming into a ferromagnetic state, the solitons act as seeds at

the fixed boundaries, evolving into isolated elongated skyrmions. The critical magnetic field for the formation of elongated skyrmions decreases with increasing temperature. When compared with solitons, the elongated skyrmions are stabilized in a relatively narrow window of magnetic field, especially at higher temperatures close to T_C . In contrast, on decreasing the magnetic field from the saturated state, the ferromagnetic domains transform directly into magnetic solitons, as a result of the large magnetic hysteresis of CrNb_3S_6 ^[47] in Figure S1, Supporting Information.

CrNb_3S_6 nanostructures with widths of 400, 600 nm, 3, and 9 μm were fabricated and used to systematically study the effect of geometric confinement on the formation and stability of elongated magnetic skyrmions, as shown in the Figures S2–S5, Supporting Information. Only the nanostructure with a width of 400 nm showed no magnetic transition. A wedge-shaped nanostructure with a continuous variation in width from 0 to 1000 nm was also fabricated. Figure 3a–e shows defocused LTEM images of the wedge-shaped nanostructure, in which the magnetic solitons transform to elongated skyrmions as a function of nanostructure width. The regions with opposite magnetic contrast are also observed in the nanostructure, as indicated by the shadowed blue box in Figure 3a–e. It is caused by the flipped crystallographic chirality in CrNb_3S_6 crystal, which has already been studied in similar helimagnets, that is, CrTa_3S_6 ^[38] and FeTa_3S_6 .^[48] In a low magnetic field, helical stripes and solitons

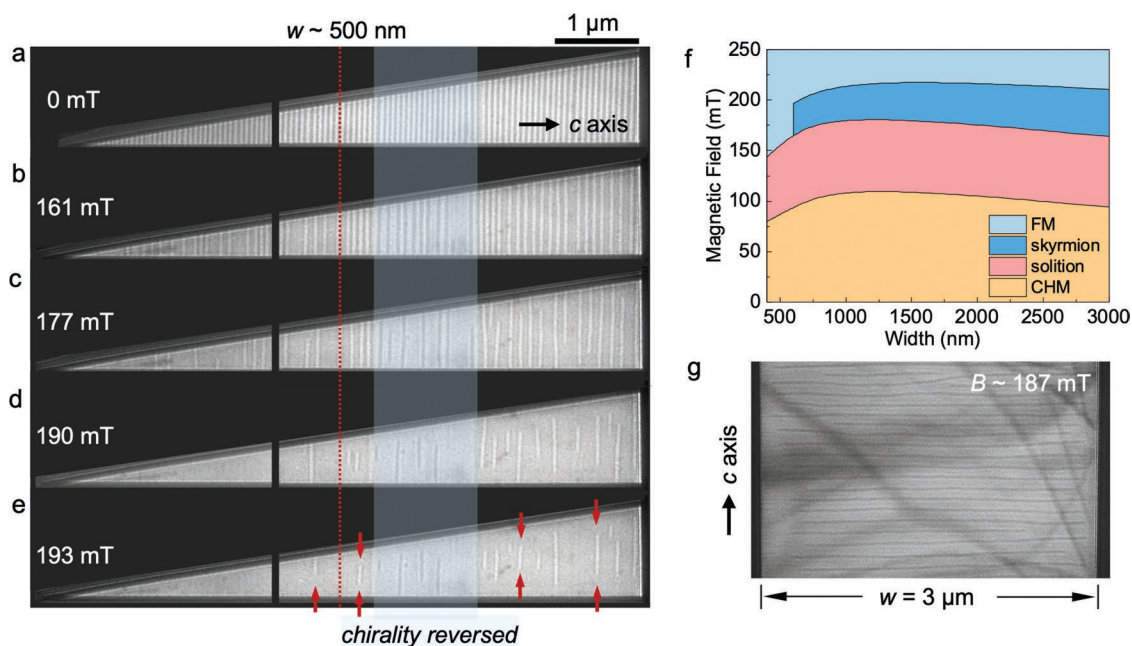


Figure 3. Width dependence of soliton-to-skyrmion transition in a wedge-shaped CrNb_3S_6 nanostripe. a–e) Magnetic-field-driven evolution of soliton-to-skyrmion transformation in a wedge-shaped nanostripe with a width of 0–1 μm in the presence of an external magnetic field. The critical width for the transformation is ≈ 500 nm, as marked by a red dotted line. The disconnected solitons are indicated by red arrows. The shadowed blue box marks the regions with opposite magnetic contrast owing to the reversal of crystal chirality. f) Magnetic phase diagram plotted as a function of magnetic field and nanostripe width. Multiple magnetic phases can be identified with increasing magnetic field, including CHM, CSL, skyrmion, and ferromagnetic states. g) Representative Lorentz TEM image of elongated skyrmions in a nanostripe with a width of 3 μm at $H = 187$ mT.

at the upper and lower side are terminated at the nanostripe edge. With increasing magnetic field, the solitons escape from the boundaries and collapse into independently elongated magnetic skyrmions. A critical width of ≈ 500 nm is identified for the soliton-to-skyrmion transition, as indicated by a red dotted line in Figure 3. Below this width, no skyrmion phase is observed. Above it, the soliton-to-skyrmion transition follows the same behavior as that described above. A magnetic phase diagram plotted as a function of magnetic field and nanostripe width is shown in Figure 3f. A typical LTEM image is shown in Figure 3g for a width of 3 μm at $H = 187$ mT.

Micromagnetic simulations were performed using a graphics processor unit (GPU)-supported micromagnetic package^[49] to understand the origin of the soliton-to-skyrmion transition and its width dependence. Although a field-dependent periodicity of magnetic solitons is observed, the elongated magnetic skyrmions are not reproduced by only considering a monoaxial DM interaction, a ferromagnetic exchange interaction, and a Zeeman energy term, even in a nanostripe with a fixed boundary. Dipolar–dipolar interactions are therefore expected to play a significant role during the magnetic phase transitions.

Figure 4a shows typical magnetic profiles for a sample with a width of 1000 nm and a thickness of 180 nm after considering dipolar–dipolar interactions. Interestingly, the magnetic soliton escapes from the edges with increasing magnetic field. The topological charge of the elongated skyrmion is calculated to be $Q = -1$. Therefore, dipolar–dipolar interactions are essential in stabilizing elongated skyrmions.^[50,51] The skyrmion becomes shorter when the external field is increased, as the magnetization at the core of the skyrmion is antiparallel to the external field.

Besides, the Lorentz–Fresnel images are simulated in Figure S6, Supporting Information, based on these magnetic profiles, consistent with the experimental observations. To clarify the difference between the magnetic solitons and elongated skyrmions, the spin configurations are plotted for comparison in Figure S7, Supporting Information. The soliton can be regarded as an infinite line and the spin textures are all the same along the soliton. In contrast, the elongated skyrmion encloses its ends by two merons, as the enlarged images extracted from the top and bottom parts. In the middle part of the elongated skyrmion, it holds the same spin configurations as the soliton. Therefore, the elongated skyrmion takes a unit topological charge. Figure 4b shows the energy density plotted as a function of CSL periodicity (L) at $H = 170$ mT in the nanostripe. There is an optimal length, at which the energy density is lowest for a specific external field. By searching for the optimal length for the CSL and skyrmion states, we obtained the lowest energy density for the CSL and skyrmion as a function of external field in Figure 4c for a sample of width 400 nm and in Figure 4d for a width of 800 nm, respectively. The CSL always has the lowest energy density in the 400-nm-width sample. However, for the sample with a width of 800 nm, the skyrmion state is the ground state if the external field is greater than 200 mT. The width-dependence of the soliton-to-skyrmion transition indicates that dipolar–dipolar interactions contribute to the stabilization of elongated skyrmions, which are not present in the narrowest nanostripe because the dipolar–dipolar interactions are more prominent in larger nanostripes. At the edge of the nanostripe, dipolar–dipolar interactions align spins parallel to the boundary, leading to the formation of elongated skyrmions to reduce magnetic charges.

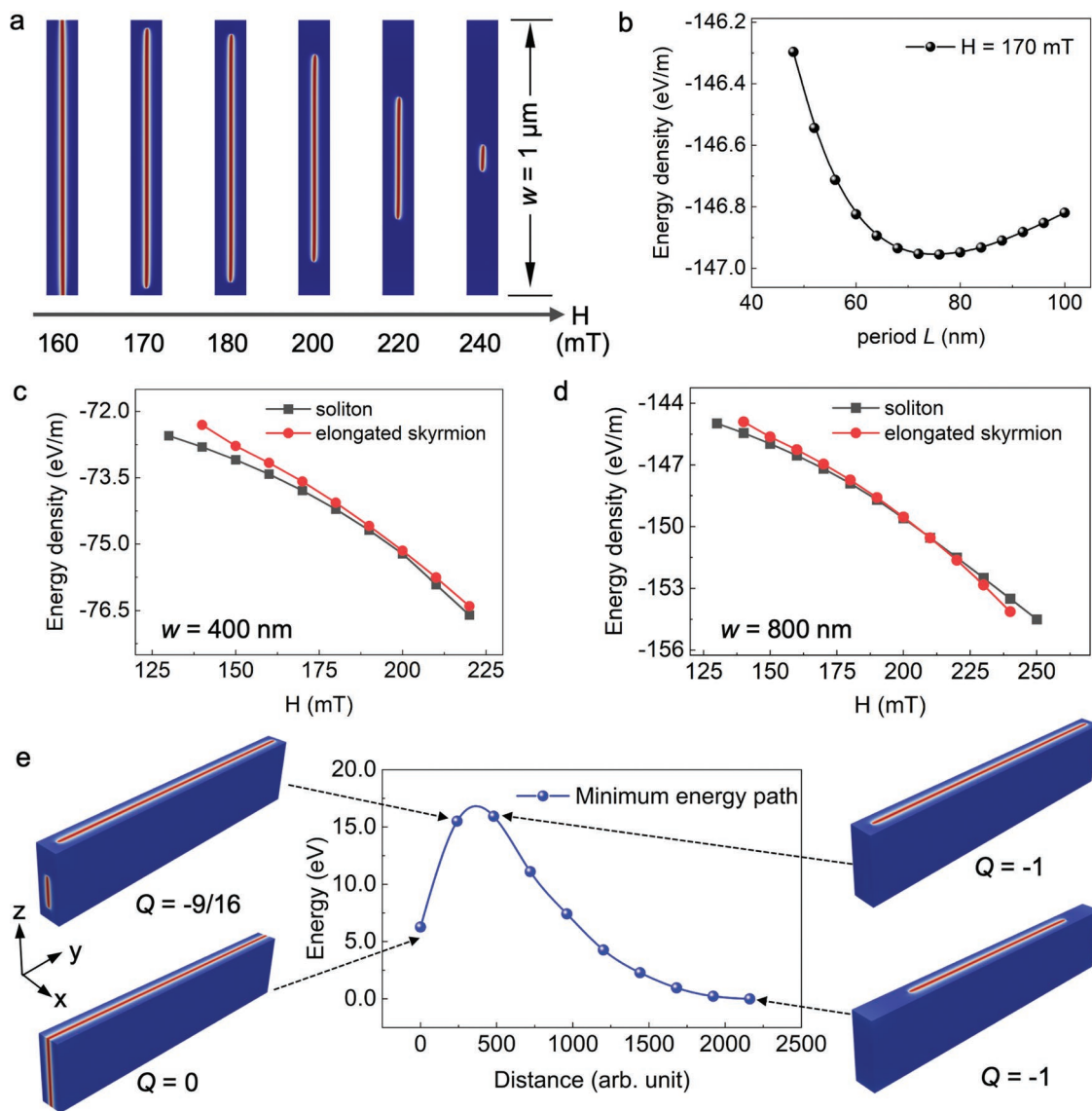


Figure 4. Micromagnetic simulations of the transformation from magnetic solitons to skyrmions. a) Evolution of magnetic configurations with increasing external magnetic field obtained by minimizing the total micromagnetic energy. The sample size used in the simulations was $60 \times 400 \times 180 \text{ nm}^3$ with periodic boundary conditions in the $+x$ direction. The CSL state ($Q = 0$) is stabilized when $H = 110 \text{ mT}$. An elongated magnetic skyrmion ($Q = -1$) is stabilized when the external field is higher than $H = 130 \text{ mT}$. b) Energy density of the skyrmion plotted as a function of CSL period L for an external field of $H = 170 \text{ mT}$. The optimal period $L = 68 \text{ nm}$. c,d) Energy densities compared between the CSL and skyrmion states for sample widths of 400 and 800 nm, respectively. The energy densities of the CSL states are always lower than those of the skyrmion states in (c), whereas the skyrmion state is the ground state when the external field is higher than 200 mT in (d). e) Calculated minimum energy path for the transition from the CSL state to the elongated skyrmion using the nudged elastic band (NEB) method. A sample with the dimension of $60 \times 800 \times 180 \text{ nm}^3$ and the periodic boundary condition in the $+x$ direction are used. The applied Zeeman field is 190 mT, under which the total energy of the CSL is larger than that for the elongated skyrmion. The typical magnetic configurations and their topological charges are shown to demonstrate the transition dynamics.

To clarify the dynamics and the variation of topological charge during the transition, we have further calculated the minimum energy path using the nudged elastic band method as shown in Figure 4e. The system with the dimension of $60 \times 800 \times 180 \text{ nm}^3$ is used and the periodic boundary condition in the $+x$ direction is applied. The applied Zeeman field is 190 mT, so the energy density of the elongated skyrmion is lower than that of the CSL state, as shown in Figure 4d. The initial CSL state with $Q = 0$ corresponds to the leftmost point in the minimum energy

path, whereas the elongated skyrmion with $Q = -1$ is shown on the right of the path. The transition from the CSL to skyrmion first occurs in the top and bottom layers of the sample, probably due to the nonuniform distribution of the demagnetization fields. Meanwhile, the nonzero topological charge of $Q = -9/16$ is obtained with the increasing total energy. Subsequently, the skyrmions grow in the thickness direction until the elongated skyrmions are fully formed in all layers with a topological charge of $Q = -1$, accompanying the decreasing total energy.

3. Conclusion

We have observed the transformation of a magnetic soliton to a magnetic skyrmion in a nanostripe of CrNb₃S₆ soliton crystal with a monoaxial DM interaction as a result of the presence of a fixed geometric boundary. We also observe width-dependent transitions, in which magnetic dipolar interactions are thought to dominate the formation of magnetic skyrmions. These inferences are confirmed by micromagnetic simulations. Our findings bring new insight into the control of magnetic transitions and into the physical characters of skyrmions and chiral solitons, thereby enriching their future spintronic applications.

4. Experimental Section

Fabrication of CrNb₃S₆ Nanostripes: A single crystal of CrNb₃S₆ was synthesized using a chemical vapor transport method. Nanostripes with various sizes were prepared for TEM observation using a lift-out method in a focused ion beam scanning electron microscope dual-beam workstation (FEI Helios Nanolab 600i) equipped with a gas injection system and a micromanipulator (Oxford Omniprobe 200). Details of the sample fabrication procedure can be found in ref. [43].

Lorentz TEM and Off-Axis Electron Holography: Lorentz–Fresnel defocus imaging and off-axis electron holography experiments were performed in magnetic-field-free conditions (Lorentz mode) at 200 kV in a Thermo Fisher Talos F200 TEM and at 300 kV in a spherical image aberration-corrected FEI Titan 60–300 TEM equipped with a Lorentz lens and an electrostatic biprism, respectively. A liquid-N₂-cooled TEM specimen holder (Gatan 636) was used to control the specimen temperature between 95 and 380 K. Electron holograms were recorded using a single electrostatic biprism and a direct electron counting camera (Gatan K2-1S). A typical voltage of 120 V was used to form an interference fringe spacing of 2.78 nm with a fringe contrast of more than 65%. Each experiment involved the acquisition of 25 object holograms, followed by 25 vacuum reference holograms to remove distortions associated with the imaging and recording system of the microscope. Averaging of the holograms, which were each acquired using an exposure time of 4 s, was used to improve the signal-to-noise ratio. Phase images were reconstructed using a standard Fourier-transform-based approach in Holoworks 6.0 software (Holowork LLC).^[52] The mean inner potential contribution was separated from the magnetic contribution by taking half of the difference between total phase shift images that had been recorded below the Curie temperature and at room temperature. The phase diagram was reconstructed by recording the magnetic states with respect to the magnetic field and temperature. At each temperature, the magnetic field was increased from 0 mT to the saturated field with the step of ≈10 mT, in order to record the full magnetic evolution process. For simplicity, the critical field for the transition from CHM to soliton phase was defined when the period of CHM was obviously increased. The critical field for the transition from soliton to skyrmion phase was defined when the first elongated skyrmion was formed. The critical field for the transition from skyrmion to ferromagnetic phase was defined when the magnetic contrast was invisible.

Micromagnetic Simulations: Micromagnetic simulations were performed using the GPU-supported micromagnetic package JuMag.^[49] The parameters used for CrNb₃S₆ were as follows: saturation magnetization $M_s = \frac{2.9\mu_B}{V/6} = 1.55 \times 10^5 \text{ A m}^{-1}$, where $V = 173.52 \text{ \AA}^3$ was the atomic volume; exchange constant $A = \frac{A_0 S^3}{4\nu_0} = 7.33 \times 10^{-13} \text{ J m}^{-2}$, where $A_0 = 106.3 \text{ meV \AA}^2$ was the spin wave stiffness constant and $S = 3/2$; 1D DMI constant $D = 4\pi A/L = 1.918 \times 10^{-4} \text{ J m}^{-1}$, where the period $L = 48 \text{ nm}$; hard axis anisotropy with $K = -1.46 \times 10^5 \text{ J m}^{-3}$. The discretization cell size was $1 \times 1 \times 5.625 \text{ nm}^3$. The energy densities both for the CSL and skyrmion states depend on the external fields as well

as the periods. In the simulations, one unit with periodic boundary conditions in the +x direction was chosen. To obtain the lowest energy density, the external fields and the unit period L_x were varied both for CSL and skyrmion states. Therefore, the lowest energy density for each external field could be obtained, as shown in Figure 4b, for $H = 170 \text{ mT}$. In this way, the lowest energy densities were obtained in Figure 4c as a function of an external field, indicated with dark dots. The same procedure was applied to calculate the energy density of skyrmion phases, as plotted in Figure 4c with red dots.

Simulation of Magnetic Phase Images: The electron optical phase shift could be written in the form

$$\varphi_M = -\frac{\mu_0 M_s L_z}{2\phi_0} \int \frac{(y-q)m_x(p,q) - (x-p)m_y(p,q)}{(x-p)^2 + (y-q)^2} dp dq \quad (1)$$

where ϕ_0 was a magnetic flux quantum and m was the magnetic moment. Spin configurations were based on output from the micromagnetic simulations. Phase images were calculated using a self-customized python code.

Supporting Information

Supporting Information is available from the Wiley Online Library or from the author.

Acknowledgements

H.D. acknowledges financial support from the National Key R&D Program of China (Grant No. 2022YFA1403603), the Chinese National Natural Science Foundation (Grant No. 12241406), the Strategic Priority Research Program of the Chinese Academy of Sciences (Grant No. XDB33030100), and the Key Research Program of Frontier Sciences, CAS, (Grant No. QYZDB-SSW-SLH009). D.S. acknowledges financial support from the Chinese National Natural Science Foundation (52173215), the Natural Science Foundation of Anhui Province for Excellent Young Scientist (2108085Y03), and the National Natural Science Fund for Excellent Young Scientists Fund Program (Overseas). F.Z., A.K., and R.E.D.-B. acknowledge funding from the European Research Council under the European Union's Horizon 2020 Research and Innovation Programme (Grant No. 856538, project "3D MAGiC") and the Deutsche Forschungsgemeinschaft (DFG, project-IDs 405553726).

Conflict of Interest

The authors declare no conflict of interest.

Data Availability Statement

The data that support the findings of this study are available from the corresponding author upon reasonable request.

Keywords

chiral soliton lattices, Dzyaloshinskii–Moriya interactions, skyrmions, topological magnetic transition

Received: October 24, 2022

Revised: December 17, 2022

Published online: March 16, 2023

- [1] I. Dzyaloshinsky, *J. Phys. Chem. Solids* **1958**, *4*, 241.
- [2] T. Moriya, *Phys. Rev.* **1960**, *120*, 91.
- [3] N. Nagaosa, Y. Tokura, *Nat. Nanotechnol.* **2013**, *8*, 899.
- [4] A. Bogdanov, A. Hubert, *J. Magn. Magn. Mater.* **1994**, *138*, 255.
- [5] A. Bogdanov, A. Hubert, *J. Magn. Magn. Mater.* **1999**, *195*, 182.
- [6] A. Fert, P. M. Levy, *Phys. Rev. Lett.* **1980**, *44*, 1538.
- [7] Y. Togawa, T. Koyama, K. Takayanagi, S. Mori, Y. Kousaka, J. Akimitsu, S. Nishihara, K. Inoue, A. S. Ovchinnikov, J. Kishine, *Phys. Rev. Lett.* **2012**, *108*, 107202.
- [8] S. K. Karna, F. N. Womack, R. Chapai, D. P. Young, M. Marshall, W. Xie, D. Graf, Y. Wu, H. Cao, L. DeBeer-Schmitt, P. W. Adams, R. Jin, J. F. DiTusa, *Phys. Rev. B* **2019**, *100*, 184413.
- [9] S. K. Karna, M. Marshall, W. Xie, L. DeBeer-Schmitt, D. P. Young, I. Vekhter, W. A. Shelton, A. Kovács, M. Charilaou, J. F. DiTusa, *Nano Lett.* **2021**, *21*, 1205.
- [10] C. Zhang, J. Zhang, C. Liu, S. Zhang, Y. Yuan, P. Li, Y. Wen, Z. Jiang, B. Zhou, Y. Lei, D. Zheng, C. Song, Z. Hou, W. Mi, U. Schwingenschlögl, A. Manchon, Z. Q. Qiu, H. N. Alshareef, Y. Peng, X.-X. Zhang, *Adv. Mater.* **2021**, *33*, 2101131.
- [11] S. Mühlbauer, B. Binz, F. Jonietz, C. Pfleiderer, A. Rosch, A. Neubauer, R. Georgii, P. Böni, *Science* **2009**, *323*, 915.
- [12] X. Z. Yu, Y. Onose, N. Kanazawa, J. H. Park, J. H. Han, Y. Matsui, N. Nagaosa, Y. Tokura, *Nature* **2010**, *465*, 901.
- [13] F. N. Rybakov, A. B. Borisov, S. Blügel, N. S. Kiselev, *Phys. Rev. Lett.* **2015**, *115*, 117201.
- [14] F. Zheng, F. N. Rybakov, A. B. Borisov, D. Song, S. Wang, Z.-A. Li, H. Du, N. S. Kiselev, J. Caron, A. Kovács, M. Tian, Y. Zhang, S. Blügel, R. E. Dunin-Borkowski, *Nat. Nanotechnol.* **2018**, *13*, 451.
- [15] D. Foster, C. Kind, P. J. Ackerman, J.-S. B. Tai, M. R. Dennis, I. I. Smalyukh, *Nat. Phys.* **2019**, *15*, 655.
- [16] J. Tang, Y. Wu, W. Wang, L. Kong, B. Lv, W. Wei, J. Zang, M. Tian, H. Du, *Nat. Nanotechnol.* **2021**, *16*, 1086.
- [17] A. K. Nayak, V. Kumar, T. Ma, P. Werner, E. Pippel, R. Sahoo, F. Damay, U. K. Rößler, C. Felser, S. S. P. Parkin, *Nature* **2017**, *548*, 561.
- [18] H. Vakili, J.-W. Xu, W. Zhou, M. N. Sakib, M. G. Morshed, T. Hartnett, Y. Quessab, K. Litzius, C. T. Ma, S. Ganguly, M. R. Stan, P. V. Balachandran, G. S. D. Beach, S. J. Poon, A. D. Kent, A. W. Ghosh, *J. Appl. Phys.* **2021**, *130*, 070908.
- [19] L. Peng, R. Takagi, W. Koshibae, K. Shibata, K. Nakajima, T. Arima, N. Nagaosa, S. Seki, X. Yu, Y. Tokura, *Nat. Nanotechnol.* **2020**, *15*, 181.
- [20] K. Karube, L. Peng, J. Masell, X. Yu, F. Kagawa, Y. Tokura, Y. Taguchi, *Nat. Mater.* **2021**, *20*, 335.
- [21] J. Jena, B. Göbel, T. Ma, V. Kumar, R. Saha, I. Mertig, C. Felser, S. S. P. Parkin, *Nat. Commun.* **2020**, *11*, 1115.
- [22] X. Z. Yu, W. Koshibae, Y. Tokunaga, K. Shibata, Y. Taguchi, N. Nagaosa, Y. Tokura, *Nature* **2018**, *564*, 95.
- [23] W. Wei, J. Tang, Y. Wu, Y. Wang, J. Jiang, J. Li, Y. Soh, Y. Xiong, M. Tian, H. Du, *Adv. Mater.* **2021**, *33*, 2101610.
- [24] X. Z. Yu, N. Kanazawa, Y. Onose, K. Kimoto, W. Z. Zhang, S. Ishiwata, Y. Matsui, Y. Tokura, *Nat. Mater.* **2011**, *10*, 106.
- [25] S. Seki, X. Z. Yu, S. Ishiwata, Y. Tokura, *Science* **2012**, *336*, 198.
- [26] T. Moriya, T. Miyadai, *Solid State Commun.* **1982**, *42*, 209.
- [27] T. Miyadai, K. Kikuchi, H. Kondo, S. Sakka, M. Arai, Y. Ishikawa, *J. Phys. Soc. Jpn* **1983**, *52*, 1394.
- [28] N. J. Ghimire, M. A. McGuire, D. S. Parker, B. Sipos, S. Tang, J.-Q. Yan, B. C. Sales, D. Mandrus, *Phys. Rev. B* **2013**, *87*, 104403.
- [29] J. Kishine, I. G. Bostrem, A. S. Ovchinnikov, V. E. Sinitsyn, *Phys. Rev. B* **2014**, *89*, 014419.
- [30] Y. Togawa, T. Koyama, Y. Nishimori, Y. Matsumoto, S. McVitie, D. McGrouther, R. L. Stamps, Y. Kousaka, J. Akimitsu, S. Nishihara, K. Inoue, I. G. Bostrem, V. E. Sinitsyn, A. S. Ovchinnikov, J. Kishine, *Phys. Rev. B* **2015**, *92*, 220412.
- [31] V. Laliena, J. Campo, J.-I. Kishine, A. S. Ovchinnikov, Y. Togawa, Y. Kousaka, K. Inoue, *Phys. Rev. B* **2016**, *93*, 134424.
- [32] J. Yonemura, Y. Shimamoto, T. Kida, D. Yoshizawa, Y. Kousaka, S. Nishihara, F. J. T. Goncalves, J. Akimitsu, K. Inoue, M. Hagiwara, Y. Togawa, *Phys. Rev. B* **2017**, *96*, 184423.
- [33] Y. Togawa, Y. Kousaka, S. Nishihara, K. Inoue, J. Akimitsu, A. S. Ovchinnikov, J. Kishine, *Phys. Rev. Lett.* **2013**, *111*, 197204.
- [34] J. Kishine, I. Proskurin, I. G. Bostrem, A. S. Ovchinnikov, V. E. Sinitsyn, *Phys. Rev. B* **2016**, *93*, 054403.
- [35] L. Wang, N. Chepiga, D.-K. Ki, L. Li, F. Li, W. Zhu, Y. Kato, O. S. Ovchinnikova, F. Mila, I. Martin, D. Mandrus, A. F. Morpurgo, *Phys. Rev. Lett.* **2017**, *118*, 257203.
- [36] S. Tang, R. S. Fishman, S. Okamoto, J. Yi, Q. Zou, M. Fu, A.-P. Li, D. Mandrus, Z. Gai, *Nano Lett.* **2018**, *18*, 4023.
- [37] R. Aoki, Y. Kousaka, Y. Togawa, *Phys. Rev. Lett.* **2019**, *122*, 057206.
- [38] K. Du, F.-T. Huang, J. Kim, S. J. Lim, K. Gamage, J. Yang, M. Mostovoy, J. Garlow, M.-G. Han, Y. Zhu, S.-W. Cheong, *Proc. Natl. Acad. Sci. USA* **2021**, *118*, e2023337118.
- [39] D. Obeysekera, K. Gamage, Y. Gao, S. Cheong, J. Yang, *Adv. Electron. Mater.* **2021**, *7*, 2100424.
- [40] A. E. Hall, J. C. Loudon, P. A. Midgley, A. C. Twitchett-Harrison, S. J. R. Holt, D. A. Mayoh, J. P. Tidey, Y. Han, M. R. Lees, G. Balakrishnan, *Phys. Rev. Mater.* **2022**, *6*, 024407.
- [41] D. A. Mayoh, J. Bouaziz, A. E. Hall, J. B. Staunton, M. R. Lees, G. Balakrishnan, *Phys Rev Res* **2022**, *4*, 013134.
- [42] C.-H. Zhang, H. Algaidi, P. Li, Y. Yuan, X.-X. Zhang, *Rare Met.* **2022**, *41*, 3005.
- [43] C. Jin, Z.-A. Li, A. Kovács, J. Caron, F. Zheng, F. N. Rybakov, N. S. Kiselev, H. Du, S. Blügel, M. Tian, Y. Zhang, M. Farle, R. E. Dunin-Borkowski, *Nat. Commun.* **2017**, *8*, 15569.
- [44] G. W. Paterson, T. Koyama, M. Shinozaki, Y. Masaki, F. J. T. Goncalves, Y. Shimamoto, T. Sogo, M. Nord, Y. Kousaka, Y. Kato, S. McVitie, Y. Togawa, *Phys. Rev. B* **2019**, *99*, 224429.
- [45] D. Song, L. Wang, W. Wang, F. Zheng, J. Tang, S. Wang, C. Zhu, J. Caron, A. Kovács, Z. Liu, D. Mandrus, M. Tian, H. Du, R. E. Dunin-Borkowski, *Phys. Rev. B* **2020**, *102*, 064432.
- [46] P. A. Midgley, R. E. Dunin-Borkowski, *Nat. Mater.* **2009**, *8*, 271.
- [47] M. Shinozaki, Y. Masaki, R. Aoki, Y. Togawa, Y. Kato, *Phys. Rev. B* **2018**, *97*, 214413.
- [48] Y. Horibe, J. Yang, Y.-H. Cho, X. Luo, S. B. Kim, Y. S. Oh, F.-T. Huang, T. Asada, M. Tanimura, D. Jeong, S.-W. Cheong, *J. Am. Chem. Soc.* **2014**, *136*, 23.
- [49] W. Wang, *JuMag—A Julia Package for Classical Spin Dynamics and Micromagnetic Simulations with GPU Support*, **2022**.
- [50] J. Lucassen, M. J. Meijer, O. Kurnosikov, H. J. M. Swagten, B. Koopmans, R. Lavrijsen, F. Kloodt-Twesten, R. Frömter, R. A. Duine, *Phys. Rev. Lett.* **2019**, *123*, 157201.
- [51] W. Legrand, J.-Y. Chauleau, D. Maccariello, N. Reyren, S. Collin, K. Bouzehouane, N. Jaouen, V. Cros, A. Fert, *Sci. Adv.* **2018**, *4*, eaat0415.
- [52] E. Voelkl, D. Tang, *Ultramicroscopy* **2010**, *110*, 447.